AIAA JOURNAL
Vol. 62, No. 12, December 2024

Interferometric Rayleigh Scattering for Flow Temperature and Velocity Analysis

Igor Kurek,* Pierre Lecomte,† Thomas Castelain,‡ Emmanuel Jondeau,§ and Christophe Bailly¶
Ecole Centrale de Lyon, CNRS, INSA Lyon, Universite Claude Bernard Lyon I, LMFA, UMR5509, 69130, Ecully, France

https://doi.org/10.2514/1.J064333

A new processing method is developed to analyze images from a Fabry–Pérot interferometer in order to extract point measurements of temperature and velocity within a gas flow, using Rayleigh scattering. Two types of interferograms are generated from a Fabry–Pérot model combined with a simulated light source. The first type is obtained from a diffuse coherent light source, namely, a laser beam on a diffuser. The interferometer characteristics, defined by only two independent parameters, are retrieved within 0.1% accuracy. The knowledge of these parameters is mandatory to analyze interferograms from Rayleigh scattered light. The second type corresponds to Rayleigh scattered light from a small volume under flow conditions, lighted with a focused laser beam and captured with long exposure time. Several flow parameters are chosen to generate these interferograms. The relative errors on the temperature and velocity estimates are found to be weak. Noise is also added to assess the robustness of the processing method. The error induced by the estimates of the instrument function is found to be of second order compared to the error induced by the image analysis.

Nomenclature

c	=	speed of light in vacuum, m/s
d	=	distance between reflective surfaces, m
f_c	=	collimating lens focal length, m
f_f	=	fringe forming lens focal distance, m
H	=	full width at half maximum of laser shape
I_{FP}	=	instrument function
$\tilde{I}_{\text{FP}}$	=	radial intensity function of reference interferogram from annular summing
I^{2D}_{FP}	=	reference modeled interferogram
l_n	=	mean free path of molecules, m
I_R	=	scattered light intensity
I_{Rayleigh}	=	Rayleigh intensity function
$\tilde{I}_{\text{Rayleigh}}$	=	radial intensity function of Rayleigh interferogram from annular summing
$\tilde{I}^{\text{th}}_{\text{Rayleigh}}$	=	theoretical radial intensity function of Rayleigh interferogram
I^{2D}_{Rayleigh}	=	Rayleigh modeled interferogram
I_{S_R}	=	broadband source of spectrum S_R intensity function
$I^{2D}_{S_R}$	=	broadband source of spectrum S_R modeled interferogram
I_0	=	incident light intensity
$\boldsymbol{K}$	=	interaction vector, m^{-1}
k_b	=	Boltzmann constant, J/K
$\boldsymbol{k}_s$	=	wave vector of the scattered light, m^{-1}
$\boldsymbol{k}_0$	=	wave vector of the incident light, m^{-1}
L	=	laser shape function
$M(X, Y)$	=	zero-mean uniform noise
m	=	mass of single molecule, kg
N	=	index of fringe
$\mathcal{N}$	=	number density, m^{-3}
$N(X, Y)$	=	noise intensity on Rayleigh interferogram
N_E	=	effective finesse
N_E^{id}	=	identified effective finesse
N_E^{in}	=	initial value of the effective finesse
$\tilde{N}$	=	average value of noise intensity on Rayleigh interferogram
P	=	pressure
p	=	pixel length, m
R_i	=	outer radius of ith annular region
R_1	=	outer radius of first annular region
r	=	distance to center of interferogram, m
r_i	=	center radius of ith annular region, m
$r_N^\star$	=	radius of N^{th} fringe, m
S_R	=	spectrum of scattered light
T	=	temperature, K
u	=	velocity (norm of $\boldsymbol{u}$), m/s
u_0	=	velocity related to thermal effect, m/s
V_s	=	sample volume
(X, Y)	=	Cartesian coordinates of interferogram, m
(X_c, Y_c)	=	coordinates of interferogram center, m
x	=	dimensionless frequency
y	=	Rayleigh scattering model parameter
γ	=	specific heat ratio
$\Delta\nu$	=	frequency shift due to bulk velocity, Hz
$\Delta\nu_T$	=	spectrum broadening due to temperature, Hz
δ	=	angle between velocity and interaction vector
κ	=	thermal conductivity, W/m/K
λ_i	=	interaction wavelength, m
λ_s	=	wavelength of scattered light, m
λ_0	=	wavelength of incident light, m
η	=	shear viscosity, Pa/s
η_b	=	bulk viscosity, Pa/s
θ	=	angle of incident light in Fabry–Pérot interferometer cavity
μ	=	refractive index
ν	=	frequency of light in vacuum, Hz
ρ	=	density, kg/m^3
σ	=	standard deviation of laser shape function
χ_s	=	scattering angle
φ	=	phase shift, rad
$\varphi(x, 0)$	=	phase shift at pattern center
φ_0	=	phase shift at pattern center for $x = 0$
φ_0^{id}	=	identified phase shift at center

Presented as Paper 2022-2957 at the 28th AIAA/CEAS Aeroacoustics Conference, Southampton, U.K., June 14–17, 2022; received 26 April 2024; revision received 24 June 2024; accepted for publication 15 July 2024; published online 23 October 2024.

*Postdoctoral Fellow; igor.kurek@ec-lyon.fr.
†Assistant Professor; pierre.lecomte@univ-yon1.fr.
‡Assistant Professor; thomas.castelain@ec-lyon.fr.
§Research Engineer; emmanuel.jondeau@ec-lyon.fr.
¶Professor; christophe.bailly@ec-lyon.fr. Senior Member AIAA.

φ_0^{in} = initial value of phase shift at center
φ_1 = phase shift of first peak

I. Introduction

THERE is continuous interest in aeroacoustics for the development and application of advanced optical methods to characterize both the velocity and temperature of a flow in a nonintrusive manner. Interferometric Rayleigh scattering (IRS) is a nonintrusive and high-frequency rate experimental technique that meets these challenges. Rayleigh scattering occurs when molecules submitted to a light electromagnetic field are excited and become secondary sources by scattering a part of this light. The intensity of the Rayleigh scattered light is directly proportional to the gas density ρ, and in low-speed flows where pressure fluctuations can usually be neglected with regard to the temperature and density fluctuations, the density can also be used to retrieve temperature fluctuations [1]. The spectral content of the scattered light provides information on bulk velocity and temperature of molecules in a given volume. Simultaneous measurement of temperature, velocity, and density [2–5] is achieved. The primary light source can be a continuous wave [2,4,6–9] or a pulsed [10–12] laser. The spectrum of Rayleigh scattered light can be retrieved by using a Fabry–Pérot interferometer [3–5,10]. The latter produces an inteferogram in the shape of concentric fringes, which is captured with a camera. Measurements are generally pointwise, but a multibeams system can allow planar measurements [13]. Density measurements from Rayleigh scattering had already been performed in the field of aeroacoustics [14,15]. The velocity and temperature fluctuations were only recently obtained using a camera, and they are still challenging to measure [16] due to particle presence and low signal-to-noise ratio, although achievable [10], but not adapted to aeroacoustic study in this case. The relative errors reported in the interferometric measurements are attributed either to the uncertainties in the geometrical or optical characteristics of the experimental setup [4] or to the analysis of the interferogram [10]. The latter is thus a crucial step. Its uncertainty sets the maximum achievable precision of the evaluation process of u and T. In the fluid mechanics field, the approach relies on analyzing the interferogram pixel by pixel [4,10,11,17]. It aims to compare the value given by each pixel to a modeled counterpart evaluated at the position of each pixels. In other domains such as aeronomy, the annular summing technique [18] is employed, which takes advantage of the circular symmetry of an interferogram. The latter is divided into several concentric regions, and the resulting averaged data are used. Each technique has its pros and cons: in the former (pixel by pixel analysis), the interferogram is directly compared to an analytical modeling, which does not take into account read noise, and shot noise from interferograms issued of short exposure time, which has different values from one pixel to the other. In the latter, using annular summing allows us to smooth the read noise effects to the expense of smoothing out the information along the width of a fringe. Nevertheless, in view of the low signal-to-noise ratio (SNR) encountered in Rayleigh scattering experiments [10,11,17], limiting as much as possible the influence of sensor noise is preferable. For this reason, we propose here evaluating the accuracy of an annular-summing-based method of Rayleigh scattering interferograms analysis.

The evaluation of the method precision can be performed by comparing experimental results obtained in a known environment, as a jet core, to their theoretical values [4,8]. In this work, the evaluation of the accuracy of the interferogram analysis method is achieved by the use of synthetic images generated from known physical models, whose input parameters are set and constitute a reference solution to the analysis output. A procedure is developed in a first part to generate synthetic interferograms on the basis of a Rayleigh scattering model described in Sec. II. In Sec. III, the IRS principle is presented, and the modeling of interferograms is developed in Sec. IV. In a second part, the analysis of interferograms is tested on these synthetic interferograms. This aims to assess the error magnitude in temperature and velocity measurements induced by the analysis process in itself, presented in Sec. V. The methodology to evaluate the robustness of the image processing algorithm is described, and results of this analysis are presented in Sec. VI. Finally, the paper concludes in Sec. VII.

II. Physical Description of Rayleigh Scattering

This section recalls the physical process of Rayleigh scattering. Rayleigh scattering describes light scattering by molecules as an elastic phenomenon which does not change the internal energy of the molecules [19]. Frequency shifts between incident and scattered light arise from translation motion of the molecules. For flow studies, the independent sources of motion are thermal agitation and bulk velocity of the molecules in the flow. The spectrum of the scattered light and its differences relatively to the spectral content of the incident light is thus representative of the molecules motion. Therefore, the analysis of the Rayleigh scattered light spectrum leads to the determination of temperature and velocity of the molecule ensemble scattering light.

The norms of the wave vector $\boldsymbol{k}_0$ of the incident light and that of the scattered light $\boldsymbol{k}$ in the observation direction are very close, with wavelengths such that $\lambda_0 \simeq \lambda$. The scattered light has a broadband spectrum, in which each frequency component can be looked at separately. The intersection between the incident light beam and the observation optical axis defines the sample volume V_s, as depicted in Fig. 1. It is sufficiently small regarding the flowfield scales that it is considered as a point. The observation angle of the scattered light is noted χ_s. The following development is based on the vector $\boldsymbol{K}$ representing the interaction between the incident and scattered waves. It is defined as the bisector of the incident and scattered light wave vectors [19], such as

$$\begin{aligned} \boldsymbol{K} &= \boldsymbol{k}_s - \boldsymbol{k}_0 \\ K = |\boldsymbol{K}| &= \frac{4\pi}{\lambda_0}\sin(\chi_s/2) \end{aligned} \tag{1}$$

The associated wavelength $\lambda_i = \lambda_0/[2\sin(\chi_s/2)]$ is referred to as the interaction wavelength. Effects of temperature or bulk motion on the scattered light spectrum are considered in the following section.

A. Gas Temperature Effects

The effect of temperature on the shape of the scattered light spectrum strongly depends on the gas regime, as expressed in the framework of the gas kinetic theory [19]. These regimes may be distinguished depending on the value of the dimensionless parameter noted y, that corresponds to the ratio between the interaction wavelength λ_i to the mean free path l_n of the molecules. Modelings of scattered light spectrum S_R such as the Tenti S6 model [20] make use of this parameter, which is expressed as

$$y = \frac{\mathcal{N} k_B T}{\sqrt{2} K u_0 \eta} \tag{2}$$

where the velocity $u_0 = \sqrt{k_B T/m}$ is related to the thermal effect, m is the mass of the molecule, $\mathcal{N}$ is the number density, k_B the Boltzmann

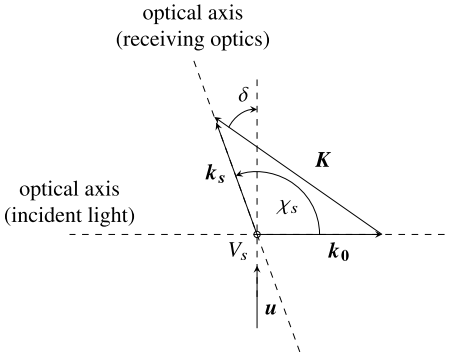

Fig. 1 Scattering vector diagram: k_0 and k are the incident and scattered light wave vectors, and u and K are the velocity and interaction vectors.

constant, and η is the shear viscosity of the gas, whose temperature dependence is expressed with the Sutherland formula [21]

$$\eta = \eta_0 \left(\frac{T}{T_0}\right)^{3/2} \left(\frac{T_0 + S}{T + S}\right) \tag{3}$$

with $\eta_0 = 1.716 \cdot 10^{-5}$ N · s/m^2, $T_0 = 273$ K, and $S = 111$ K.

Spectral line shapes in the different regimes ($y = 0.59$, $y = 0.80$, and $y = 1.15$), at atmospheric pressure, predicted by the S6 model with $\lambda_0 = 532$ nm, are shown in Fig. 2. The first regime is called Knudsen regime, or collisionless regime. The mean free path of molecules is larger than the interaction wavelength; therefore, $y \ll 1$. It corresponds to low density or high temperature of the gas. In this regime, the uncorrelated thermal motion of molecules provides a spectrum which has a Gaussian shape. This is called the thermally broadened Rayleigh line. The scattering reflects the motion of the molecules. For a gas of absolute temperature T in the Knudsen regime, the expression for the spectrum broadening due to temperature is given by the full width at half maximum (FWHM) of the Gaussian line shape $\Delta\nu_T$ [19]

$$\Delta\nu_T = \frac{K}{2\pi}\sqrt{\frac{8k_B T \ell_n(2)}{m}} \tag{4}$$

The second regime corresponds to the kinetic regime associated with high pressure or low temperature. A shorter mean free path is expected, which thus becomes of the same order as the interaction wavelength, corresponding to y close to unity. In this regime, density fluctuations begin to contribute to the spectral shape. The origin of these density fluctuations is generally acoustic waves inside the probed volume. This makes side bands, named Brillouin–Mandel'shtan scattering lines, appear. In this work, and in most aerodynamic applications, the gas regime falls into the kinetic regime [4,22]. This justifies the uses of a scattering model which can transcribe the features of the spectral shape.

The third and last regime starts when the interference length λ_i is greater than the mean free path. This is the hydrodynamic regime, for which y is greater than unity. The spectrum of the scattered light is then composed of three peaks having a Lorentzian shape. The acoustic sidebands are located at the frequency shift associated with the speed of sound in the media. Because the speed of sound is related to the temperature, these sidebands can be used to determine the temperature in the flow. The central peak is associated with the thermal diffusion rate, and is also of importance, because the ratio of the total central peak intensity to the total sidebands intensity, for a single component gas, is $\gamma - 1$, γ being the specific heat ratio.

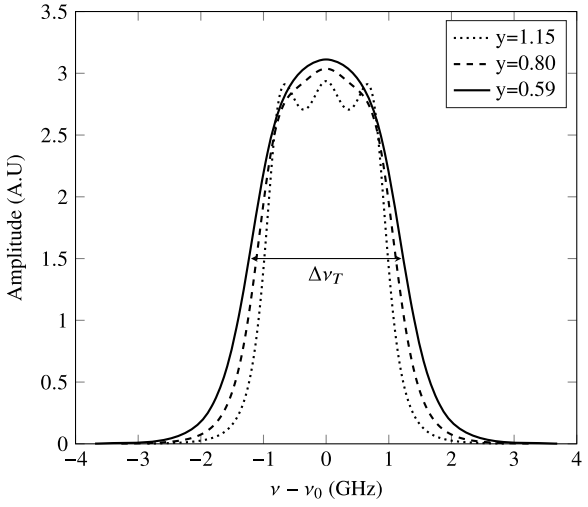

Fig. 2 Spectral line shape centered on the laser frequency of Rayleigh scattering in air at atmospheric pressure, calculated with the S6 model (solid line: $T = 373$ K ($y = 0,59$); dashed line: $T = 293$ K ($y = 0,80$); dotted line: $T = 223$ K ($y = 1.15$)). The FWHM of the spectrum in the Knudsen regime (horizontal line) is noted $\Delta\nu_T$.

In the S6 model, the frequency of the scattered light ν is normalized and expressed as a dimensionless frequency x, defined as

$$x = \frac{2\pi(\nu - \nu_0)}{\sqrt{2}Ku_0} \tag{5}$$

which is centered at the frequency of the incident light $\nu_0 = c/\lambda_0$, with c the speed of light in the vacuum. This normalization expresses the frequency with regard to its shift compared to the incident light frequency ν_0.

Air is considered as an effective single-component gas with temperature-scaled values for the relevant macroscopic transport coefficients [23]. The spectral shape of the modeled scattered light depends on the gas temperature T only.

B. Flow Velocity Effects

In addition to small-scale motion related to temperature effects, bulk motions related to convection of molecules occur for a gas flow. Molecular convection results in a frequency shift of the entire scattered light spectrum. This frequency shift $\Delta\nu$ can be expressed by the scalar product

$$\Delta\nu = \frac{1}{2\pi}\boldsymbol{u} \cdot \boldsymbol{K} \tag{6}$$

with $\boldsymbol{u}$ being the flow velocity. Using the angle δ between $\boldsymbol{u}$ and $\boldsymbol{K}$, as illustrated in Fig. 1, the frequency shift can be recast as

$$\Delta\nu = \frac{2u}{\lambda_0}\cos(\delta)\sin(\chi_s/2) \tag{7}$$

For a practical setup where $\chi_s = 90$ degree and $\boldsymbol{K}$ is colinear with $\boldsymbol{u}$, as considered in this work, the previous relationship becomes

$$\Delta\nu = \frac{\sqrt{2}}{\lambda_0}u \tag{8}$$

The definition of the dimensionless frequency x is thus updated to take into account this frequency shift, leading to

$$x = \frac{2\pi(\nu^* - \nu_0)}{\sqrt{2}Ku_0} \tag{9}$$

where $\nu^* = \nu + \Delta\nu$. As illustrated in Fig. 3, this frequency shift induced by bulk motion uniformly affects the whole spectrum, shifted in frequency by $\Delta\nu$.

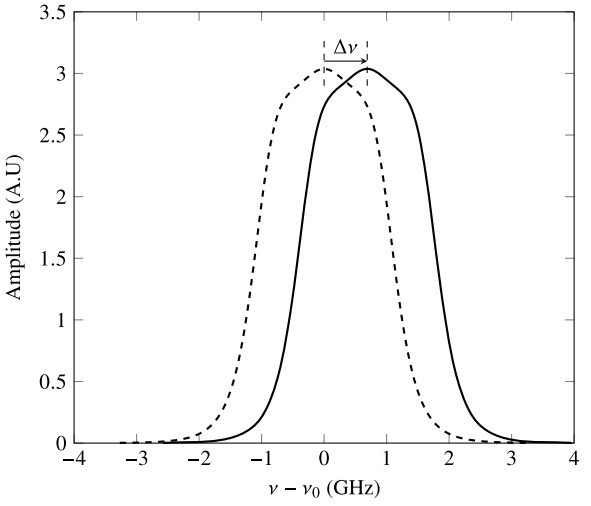

Fig. 3 Rayleigh spectrum calculated with the Tenti S6 model for air at $T = 293$ K, atmospheric pressure and $\lambda_0 = 532$ nm. The Doppler shift corresponds to a bulk velocity of 260 m/s[1] (A.U, arbitary units).

Introducing the wavelength of the scattered light under this bulk motion, $\lambda = c/\nu^*$, Eq. (9) can be recast to express the ratio between the wavelength λ_0 of the incident light and λ

$$\frac{\lambda}{\lambda_0} = \left(1 + \frac{\sqrt{2}Ku_0}{2\pi\nu_0}x\right)^{-1} = f(x) \tag{10}$$

Finally, the spectrum S_R of Rayleigh scattered light from molecules in a flow of known chemical properties does only depend on two parameter, x and y. By extension, a given spectrum $S_R(x, y)$ corresponds to a unique couple of values for u and T. The scattered light spectrum gives the opportunity to retrieve the velocity u and the temperature T of the scattering molecules. The following part focuses on the modeling of interferograms obtained from various light sources, including Rayleigh scattering.

III. Interferometric Rayleigh Scattering

With the IRS method, signals are recorded under the form of interferograms, which are images containing a set of concentric fringes around the optical axis. The IRS method relies on a parallel mirrors Fabry–Pérot interferometer (FPI), which allows high-frequency resolution, in an optical setup used in direct imaging experiments [4,10,11,24] corresponding to that displayed in Fig. 4. This setup implies a collimation lens of focal length f_c at the focus of the object plane and a fringe forming lens of focal length f_f at the focus of the image plane. The image and object plane are thus optically conjugated. The FPI is placed between the two lenses. This section presents how the physical parameters of the interferometer and the light source spectrum influence the interferogram shape. The principle of IRS is first recalled, as is the modeling of the FPI leading to the definition of its instrument function. This theoretical framework is used in Sec. IV to build synthetic interferograms that will be used in following sections to assess the analysis accuracy.

A. Principle of Interferometric Rayleigh Scattering

The FPI acts as a narrow bandpass filter and forms interferograms. A modeled interferogram from a monochromatic source of uniform intensity in the object plane is shown in Fig. 5a. The fringes are thin and are representative of the sharpness of the interferometric filter. For comparison and illustration purposes, a modeled interferogram obtained with a light source uniformly distributed in the object plane and with a spectral content corresponding to $S_R(x, 0.8)$ (as defined in Sec. II.A) is shown in Fig. 5b. The fringes are broader than with a monochromatic source. A modeled interferogram referred to as Rayleigh interferogram is displayed in Fig. 5c. In this case, the light source in the object plane is a laser beam; thus, only a portion of the image plane, whose dimensions depend on the laser beam width, is lit up. Therefore, in comparison with Fig. 5b in which circular broad fringes are observed, only portions of broad fringes are obtained in Fig. 5c.

Before considering Rayleigh interferograms, the analysis will first be focused on interferograms obtained with a uniformly distributed light source. In such cases, the circular symmetry of interferograms allows us to express them in terms of light intensity I according to the radial distance r to the interferogram center. The intensity function $I_{\mathrm{FP}}(x, r)$ is the response of the interferometer to a monochromatic source of normalized frequency x [Eq. (9)] and will be referred to as instrument function in what follows. For a source of spectrum S_R, the intensity function $I_{S_R}(r)$ is the convolution of the spectrum of the source and the instrument function

$$I_{S_R}(r) = \int_{-\infty}^{\infty} S_R(x, y) I_{\mathrm{FP}}(x, r)\,\mathrm{d}x \tag{11}$$

The goal of IRS is to determine the spectrum $S_R(x, y)$ from the Rayleigh scattering interferogram, leading to the knowledge of u and T (Sec. II). For that purpose, the instrument function $I_{\mathrm{FP}}(x, r)$ must be determined. The following part exposes the analytical relationships of the FPI which are developed toward a practical analysis of an interferogram from a monochromatic source to identify $I_{\mathrm{FP}}(x, r)$.

B. Fabry–Pérot Interferometer Instrument Function

The aim here is to recall the physical parameters determining the instrument function and to establish the expression of reduced parameters that will be used in the following. The FPI is composed of two parallel mirrors facing each others, separated by a distance d. The refractive index of the medium between the mirrors is μ. An extensive description of the instrument and underlying theoretical development can be found in Ref. [25]. In the object plane, we consider a uniform light source of spectrum S_R. We focus on a particular frequency component x of the spectrum, corresponding to a given wavelength $\lambda(x)$. As displayed in Fig. 4, any light ray radiated by a point in the object plane passes through the collimation and enters the FPI with an angle θ with respect to the optical axis. At each reflection, a part of the light ray is transmitted out of the mirror, and the rest is reflected back into the FPI. The rays exiting the FPI with the same angle θ and different phases shifts pass through the fringe forming lens of focal length f_f and are focused in the image plane on a point at a distance r of the optical axis. The light intensity at this point depends on the rays interferences with respect to their phase shift. The resulting phase shift on the image plane Φ can be expressed [25] as function of the angle θ of the incident light ray and approximated using second-order Taylor series

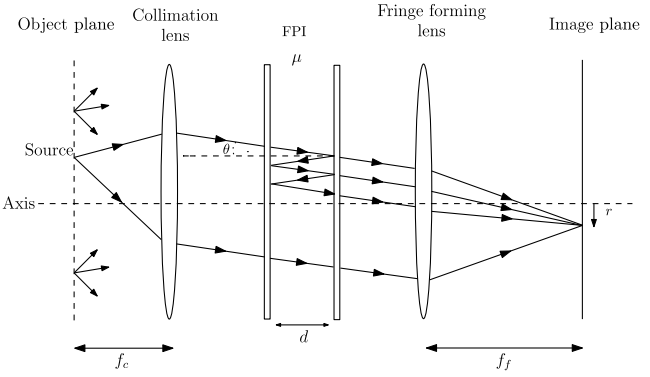

Fig. 4 Optical setup including a FPI and collimation and focusing lenses. Only the rays contributing to the interferogram are shown.

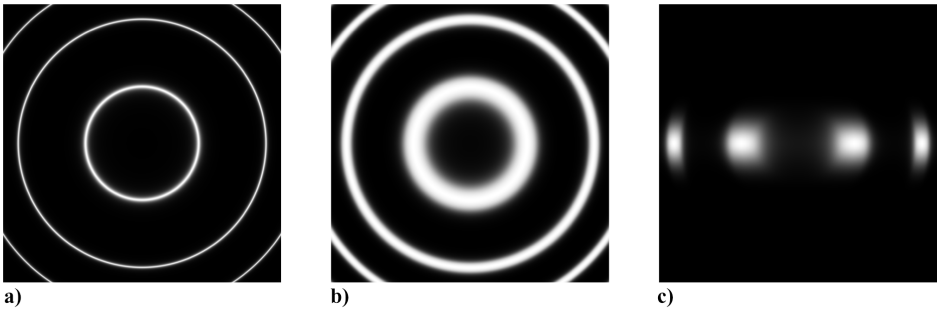

a) b) c)

Fig. 5 Fabry–Pérot interferograms from a) a monochromatic source, b) source of spectrum $S_R(x, 0.8)$, and c) focused laser Rayleigh scattered light.

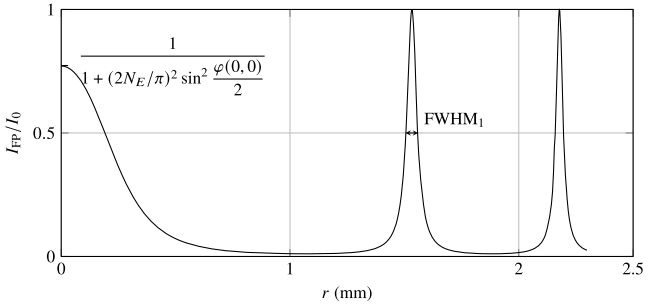

Fig. 6 Intensity function as a function of the radius from interferogram center; $N_E = 16$ and $\varphi(0,0) = 4.71 \times 10^5$.

$$\Phi = \frac{4\pi\mu d}{\lambda(x)}\cos\theta \simeq \frac{4\pi\mu d}{f(x)\lambda_0}\left[1 - \frac{1}{2}\left(\frac{r}{f_f}\right)^2\right] = \varphi(x,r) \tag{12}$$

This allows us to introduce the phase shift function $\varphi(x, r)$, which is recast as

$$\varphi(x,r) = \varphi(x,0)\left[1 - \frac{1}{2}\left(\frac{r}{f_f}\right)^2\right] \tag{13}$$

where $\varphi(x, 0)$ is the phase shift on the optical axis, that is, for $\theta = 0$ or $r = 0$.

The instrument function, denoted I_{FP}, is expressed as [25]

$$I_{FP}(\varphi) = I_0\left[1 + (2N_E/\pi)^2\sin^2(\varphi/2)\right]^{-1} \tag{14}$$

where I_0 is the incident intensity and N_E is the effective finesse defined as the ratio between 2π and the FWHM of $I_{FP}(\varphi)$. Finally, inserting Eq. (13) into Eq. (14), the instrument function $I_{FP}(x, r)$ can be expressed using $\varphi(x, 0)$ and N_E as

$$I_{FP}(x,r) = \frac{I_0}{1 + (2N_E/\pi)^2\sin^2(\varphi(x,0)[1 - (1/2)(r/f_f)^2]/2)} \tag{15}$$

Figure 6 shows $I_{FP}(0, r)$. For sufficiently high values of r, marked peaks can be noticed in this graph and correspond to the sharp fringes in the reference interferogram (Fig. 5a).

Therefore, a Fabry–Pérot interferogram only depends on two dimensionless parameters: N_E and $\varphi(x, 0)$. The following section exposes the synthesis of interferograms, based on this model.

IV. Interferogram Synthesis

In this section, the interferogram synthesis is presented. The generated interferograms will be used in Sec. VI to assess the robustness of the analysis process. The aim is to assess the maximum achievable precision of the analysis process. To get closer to the analysis of experimental interferograms, we will take into account the effects of spatial integration on the sensor with respect to its resolution and model acquisition noise by reducing it to read noise. We will be considering interferograms with long exposure times, so the effect of shot noise can be neglected. Any other uncertainties linked to the acquisition of real interferograms (geometric distortion, aberrations, etc.) will not be modeled. Unsteady behaviors are not taken into account and are out of the scope of this work. Two types are generated: reference interferograms used to determine the instrument function and Rayleigh interferograms used to retrieve the flow parameters u and T. The Rayleigh interferograms are derived from broadband synthetic interferograms. The synthesis is done by expressing the variable r in Eq. (15) in a Cartesian coordinate system where $r = \sqrt{X^2 + Y^2}$ and whose origin is located on the optical axis.

A. Reference Interferogram

Interferograms from a monochromatic light source of wavelength λ_0, uniform over the object plane, are first considered. They are defined as the images generated from the instrument function I_{FP}, defined in Eq. (15), as follows wupress the:

$$I^{2D}_{FP}(X,Y) = I_{FP}\left(0, \sqrt{X^2 + Y^2}\right) \tag{16}$$

This approach was used to generate the interferogram of Fig. 5a.

B. Broadband Interferogram

In the case of a light source of spectrum S_R, spatially uniform over the object plane, the intensity function defined in Eq. (11) is used. Then, this image is generated as previously

$$I^{2D}_{S_R}(X,Y) = I_{S_R}\left(\sqrt{X^2 + Y^2}\right) \tag{17}$$

An interferogram generated in this manner is shown in Fig. 5b.

C. Rayleigh Interferogram

Now, the case considered is that where the light source is a molecule ensemble scattering light from a laser beam. The two specific features in this case are 1) the low scattered light intensity inducing a higher sensitivity to measurement noise and 2) the spatial distribution of the laser beam light source inducing a spatial weighting in the interferogram. The former is modeled as a two-dimensional (2D) uniform noise function $N(X, Y)$ to simulate camera sensor noise such as

$$N(X,Y) = \frac{I_R}{\mathrm{SNR}}M(X,Y) + N_F \tag{18}$$

where I_R is the intensity of the scattered light, $M(X, Y)$ is a zero-mean uniform noise, and N_F is a constant simulating the noise floor level. As long time exposure interferograms are considered, shot noise contribution is considered negligible [7]. To model the spatial weighting on the interferogram, a laser beam intensity function W in the image plane is introduced. It is uniform in the X direction parallel to the beam and has a Gaussian distribution in the Y direction perpendicular to the beam, which is expressed as

$$W(Y) = 2\sqrt{2\pi}\sigma\exp\left(\frac{-Y^2}{2\sigma^2}\right) \tag{19}$$

where σ is the standard deviation of the Gaussian distribution. Finally, the intensity distribution W can be seen as a weighting on an interferogram based on a broadband source [Eq. (17)] whose spectrum corresponds to Rayleigh scattering, as described in Sec. II. The Rayleigh interferogram is then given by

$$I^{2D}_{\mathrm{Rayleigh}}(X,Y) = I_R W(Y)\int_{-\infty}^{\infty} S_R(x,y)I_{FP}\left(x, \left(\sqrt{X^2 + Y^2}\right)\right)\mathrm{d}x + N(X,Y) \tag{20}$$

To simulate the image captured by a digital camera, Eqs. (16), (17), and (20) are evaluated on a rectangular grid which mimics the sensor grid of given size and resolution Res in pixels per millimeter.

To summarize the whole process, a block diagram of the modeling and synthesis of interferograms is displayed in Fig. 7. The inputs of the modeling are listed on the left. The blue boxes on the left list the optical components and parameters needed to define the instrument function [Eq. (15)] and evaluate the FPI response to a monochromatic source as described in Sec. III.B. The green path leads to the Rayleigh intensity function following the procedure detailed in Sec III.A. A spectrum S_R is generated with the Tenti S6 model, corresponding to prescribed values of T and u as described in Sec. II. The intensity function $I_{S_R}(r)$ is then generated following Eq. (11). The paths in red represent the modeling of the 2D images. First, the mesh is defined using the camera sensor resolution Res and sensor size. The reference

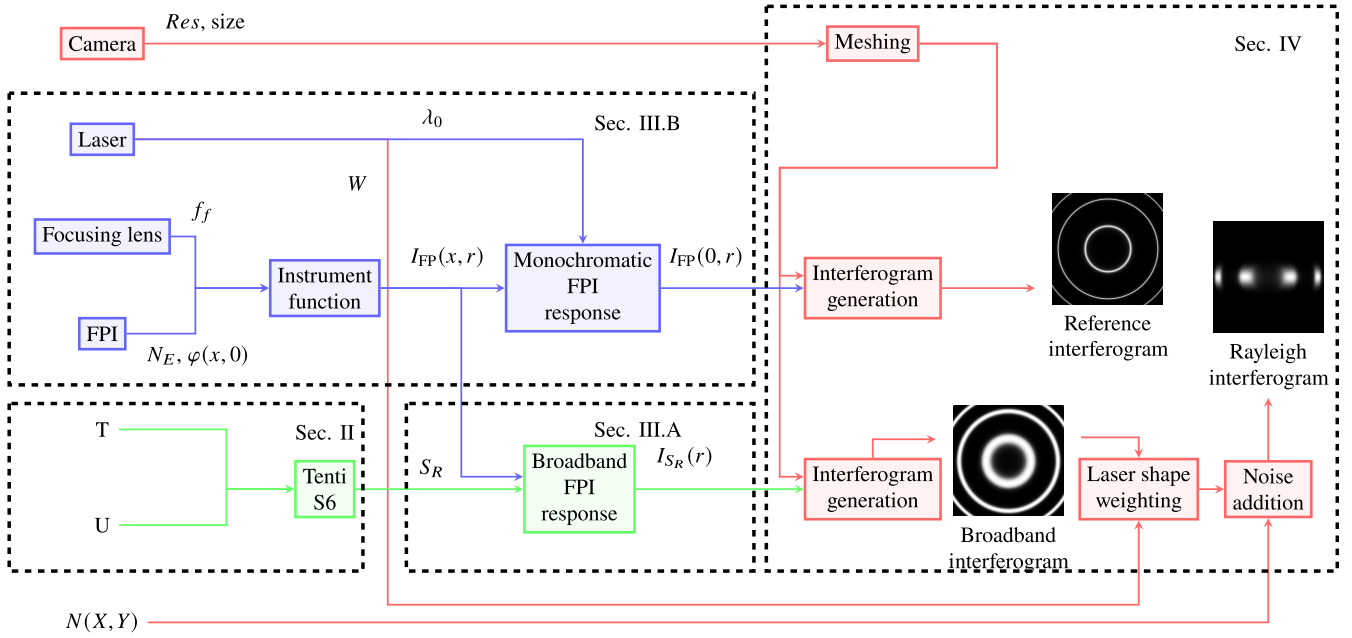

Fig. 7 Modeling of the reference and Rayleigh interferograms.

interferogram is obtained using a procedure denoted *interferogram generation*, taking as input the instrument function I_{FP} and applying Eq. (16). The same procedure but with an input corresponding to I_{S_R} is also used, to generate the interferogram corresponding to a broadband light source. Combined with the weighting function of Eq. (19), it gives the Rayleigh interferogram.

V. Interferogram Analysis

Experimentally, interferograms are captured using a camera placed in the image plane of Fig. 4. They depend on physical parameters related to the FPI that are prone to drift over time or subject to uncertainties. The FPI spacing d between the mirrors is usually known within 0.01 mm precision without considering a possible tilt angle of the mirrors due to a manufacturing defect. Uncertainties on d and μ, marginally on λ_0, and their drift over time lead to relative changes on the phase shift $\varphi(x, 0)$. In addition, the value of the finesse N_E needs to be measured in an experimental context. Indeed, a defect of parallelism between the mirrors, a slight misalignment of the optical axis, or a focusing error for instance can alter its value. The variation of ambient temperature imposes a day-to-day determination of the instrument function. The analysis procedure developed here, for use on experimental interferograms, is tested against synthetic interferograms generated as described in Sec. IV. The analysis of Rayleigh interferograms is achieved here in two steps. First, the FPI parameters N_E and $\varphi(x, 0)$ are found by analyzing an interferogram from a monochromatic source of wavelength λ_0, similar to that shown in Fig. 5a. Then, knowing these parameters, the Rayleigh interferogram can be analyzed, to obtain the flow parameters. The present section gives insights to practical considerations for interferograms analysis. The procedure to obtain the radial intensity function from the interferogram is explained, followed by the determination of the FPI parameters, and finally the estimation of the flow parameters.

A. Annular Summing of Interferograms

The idea of the present analysis is to derive from any interferogram (2D images) the related intensity function. The coordinates of the interferogram center (X_c, Y_c) are first determined. Then, the interferogram is averaged over concentric annular regions to reduce the dimension of the data set [18,26] and measurement noise footprint.

1. Center Detection

To determine the interferogram center, the following procedure is performed. A binary filter is applied to the interferogram, with a threshold at half intensity. First, the Hough transform for circle detection [27] is applied to the binary (i.e., black and white) image. This algorithm is applied to each of the first three fringes, and the average center coordinates provide the input value for an optimization procedure. The image is then converted into a one-dimensional data set: pixel intensity (in gray level) as a function of radial distance from the center, producing a discretized version of the plot shown in Fig. 6 with scattered points, as depicted in Fig. 8. The dispersion is strong if the error on the center detection is large. The optimization procedure is constituted by two steps. At half intensity, the width of the first peak is evaluated for several center guesses on an interrogation grid, with a step size of 1/10 pixel length and centered on the value provided by the Hough transform. The center guess providing the smallest value of the FWHM, defined as (*i*) in Fig. 8, is selected. In the second step, this value is used as the center of a refined interrogation grid, with a step size of 1/40 pixel length, on which the points dispersion on the rising edge of the first peak is evaluated as illustrated by (*ii*) in Fig. 8. The standard deviation of the first 200 points from the half maximum on the innermost part of the first peak is determined. The coordinates that provide the smallest value of this quantity define the center coordinates of the interferogram. As an example, Fig. 8 shows the intensity of each pixels, as a function of their distance from the center, from a badly detected center, in black. A similar plot is shown in the same figure for

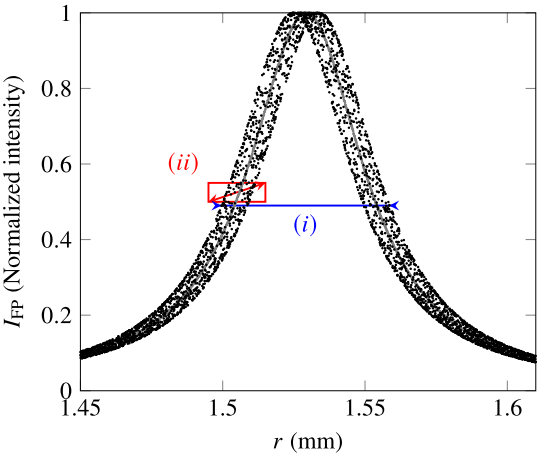

Fig. 8 Illustration of parameters (i) and (ii) used for determining interferogram center. Same instrument function parameters as in Fig. 6.

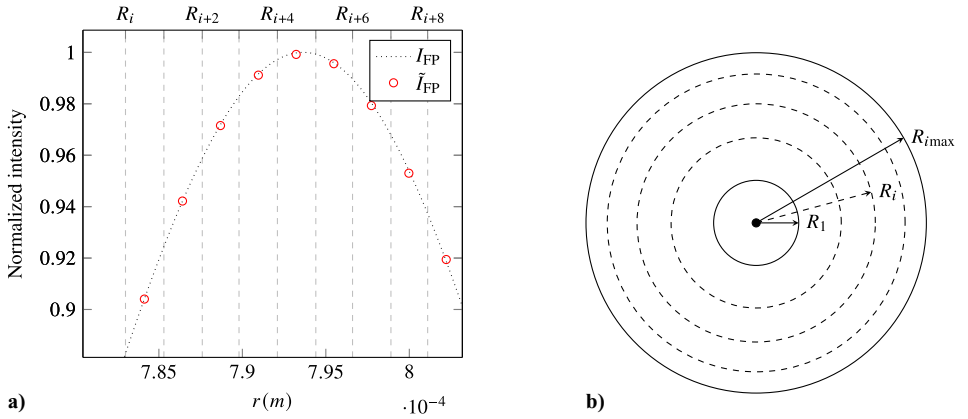

Fig. 9 Schematic representation of annular summing procedure: a) Representative I_{FP} around the first peak and averaged values $\tilde{I}_{FP}$ from the annular summing and b) schematic of the concentric regions.

the center obtained with the optimization procedure, in gray. This one-dimensional (1D) data set is used in the annular summing procedure.

2. Annular Summing

The objective is to average the interferogram over concentric annular regions of the same area, as in Fig. 9a. Therefore, the outer radius R_i of the annulus i is defined by

$$R_i = \sqrt{i} R_1 \tag{21}$$

where R_1 is the radius of the first circular region as shown in Fig. 9b. This amounts to averaging the 1D data by slices between two radii R_i and R_{i+1}. The radius r_i to which the averaged data are attributed is

$$r_i = (R_{i+1} + R_i)/2 \tag{22}$$

The radial intensity functions obtained after annular summing are denoted $\tilde{I}_{FP}(r_i)$ and $\tilde{I}_{Rayleigh}(r_i)$ for the reference and Rayleigh interferograms, respectively.

B. Determination of Instrument Function

A procedure is carried out to find out the two instrument function parameters $[\varphi(x,0), N_E]$, based on a minimization between the input reference interferogram $\tilde{I}_{FP}$ and I_{FP}. The parameter $\varphi(x,0)$ is not found directly but deduced from $\varphi(0,0) = \varphi(x,0)/f(x)$ from Eqs. (10) and (12). To simplify, we define for the latter $\varphi_0 = \varphi(0,0) \in \mathbb{R}^*$. A first estimate of the set (φ_0, N_E), used as input values for the minimization procedure, is determined by analyzing the reference interferogram. Using Eq. (13), the phase shift of the Nth peak, $N \in \mathbb{N}^*$, is noted φ_N, introducing $r_N^\star$ such as $\varphi_N = \varphi(0, r_N^\star)$. It is a multiple of 2π and can be expressed from the phase shift of the first peak φ_1 as

$$\varphi_N = \varphi_1 - 2(N-1)\pi \tag{23}$$

Then, φ_1 is expressed using Eq. (13)

$$\varphi_1 = \varphi_0 - \frac{\varphi_0}{2}\left(\frac{r_1^\star}{f_f}\right)^2 \tag{24}$$

Similarly,

$$\varphi_N = \varphi_0 - \frac{\varphi_0}{2}\left(\frac{r_N^\star}{f_f}\right)^2 \tag{25}$$

Replacing φ_N in Eq. (25) from its expression in Eq. (23) leads to

$$\varphi_1 - 2(N-1)\pi = \varphi_0 - \frac{\varphi_0}{2}\left(\frac{r_N^\star}{f_f}\right)^2 \tag{26}$$

And substituting φ_1 in Eq. (26) by its expression in Eq. (24), we obtain

$$\varphi_0 - \frac{\varphi_0}{2}\left(\frac{r_1^\star}{f_f}\right)^2 - 2(N-1)\pi = \varphi_0 - \frac{\varphi_0}{2}\left(\frac{r_N^\star}{f_f}\right)^2$$
$$\varphi_0 = \frac{4(N-1)\pi}{(r_N^\star/f_f)^2 - (r_1^\star/f_f)^2} \tag{27}$$

which allows us to determine φ_0 from the radii of the successive fringes

As demonstrated in Appendix, the relation linking the interferometer finesse to the FWHM of the radial intensity function I_{FP} on the first fringe, noted FWHM_1 and drawn in Fig. 6, is

$$N_E = \frac{\pi}{2\sin\left[(\varphi_0/4)\left(r_1^\star \mathrm{FWHM}_1/f_f^2\right)\right]} \tag{28}$$

The effective finesse value is usually lower than the finesse provided by the manufacturer, calculated using the mirror reflectivity, by a few units, corresponding to a relative change of typically 10%.

The instrument function $I_{FP}(0, r_i)$ is first evaluated at the locations r_i with these estimates of φ_0 and N_E noted φ_0^{in} and N_E^{in}, respectively. The nonlinear least-square minimization procedure lsqnonlin with the Levenberg–Marquardt algorithm from MATLAB® is used to increase the accuracy on the estimation of the parameters (φ_0, N_E) and minimizes the difference between the analyzed intensity function and $I_{FP}(0, r_i)$. The procedure is started with first guesses as in [4]

$$\min_{\varphi_0, N_E}\left(\sum_{i=1}^{i\max}\left(\tilde{I}_{FP}(r_i) - I_{FP}(0, r_i)\right)^2\right) \tag{29}$$

The input parameters are the phase shift φ_0, the effective finesse N_E, and the incident intensity I_0, whose value is the maximum intensity. The parameters identified with this procedure are noted with the superscript id, namely, φ_0^{id} and N_E^{id}.

C. Rayleigh Interferogram Analysis

The analysis of the Rayleigh interferogram first requires cropping the interferogram to retain the image partition where data are available. The remaining part after cropping, called hereafter the truncated interferogram, corresponds to a rectangle centered on the image of the laser beam that would be obtained on the image plane if the FPI were removed. Following the procedure described in Sec. V.A, this truncated interferogram gives the one-dimensional data set $\tilde{I}_{Rayleigh}(r_i)$. The temperature T and velocity u are found, as for the instrument function, with a nonlinear least-square minimization, which is expressed as

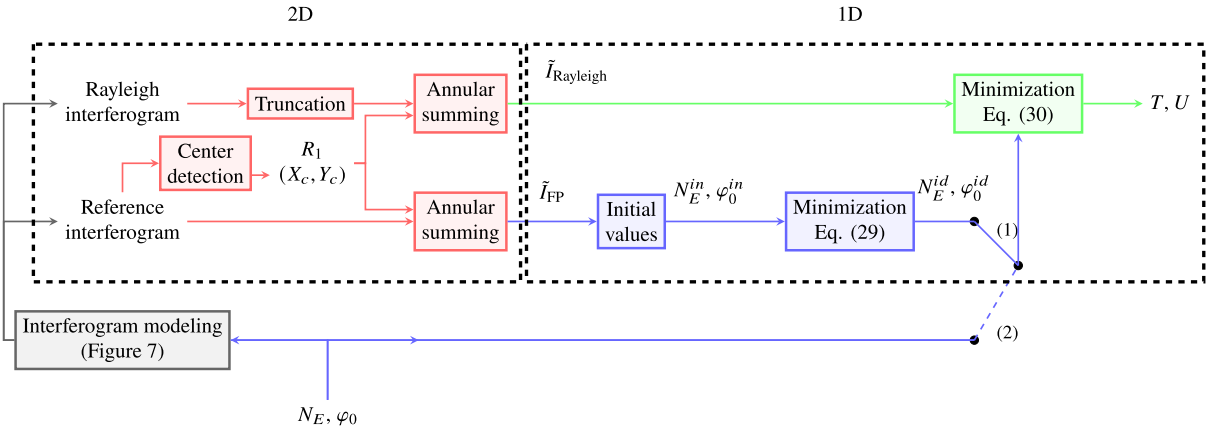

Fig. 10 Analysis of the reference and Rayleigh interferograms.

$$\min_{T,u,\tilde{I}_R,\tilde{N}} \left(\sum_{i=1}^{i\max} \left(\tilde{I}_{\text{Rayleigh}}(r_i) - \tilde{I}^{\text{mod}}_{\text{Rayleigh}}(r_i) \right)^2 \right) \tag{30}$$

During the minimization, a modeled intensity function $\tilde{I}^{\text{mod}}_{\text{Rayleigh}}$ is computed from the convolution with a modeled spectrum $S_R(x, y)$, corresponding to a unique couple of values for T and u, and the reconstructed instrument function $I_{\text{FP}}(x, r_i)$

$$\tilde{I}^{\text{mod}}_{\text{Rayleigh}}(r_i) = \tilde{I}_R \int_{-\infty}^{\infty} S_R(x, y) I_{\text{FP}}(x, r_i)\, \mathrm{d}x + \tilde{N} \tag{31}$$

where $\tilde{I}_R$ is the resulting maximum intensity of the scattered light from the truncation and annular summing procedures. It is computed at each iteration for varying T, u, and intensities $\tilde{I}_R$ and $\tilde{N}$. The spectrum S_R is computed using the Tenti S6 model from the MATLAB® transcription of the FORTRAN® code of Pan et al. [28]. The annular summing procedure averages the sensor noise $N(X, Y)$, which is assumed to have a constant mean, close to zero in this case, in each concentric region. It is then reduced to a constant value $\tilde{N}$ identical for every r_i.

A block diagram of the analysis process is shown in Fig. 10. The procedures carried out on the 2D images are represented in red. First, the center of the reference interferogram is detected. Its coordinates (X_c, Y_c) are the same for the Rayleigh and reference interferograms. The Rayleigh interferogram is truncated, keeping only the circle arcs around the maximum intensity. Then, the truncated Rayleigh interferogram and the reference interferogram are reduced to 1D data sets using the annular summing procedure described in Sec. V.A. The initial values N_E^{in} and φ_0^{in} are first found using Eqs. (28) and (27). Using the least-squares minimization corresponding to Eq. (29), the parameters of the instrument function N_E^{id} and φ_0^{id} are identified. Finally, the second least-squares minimization is performed as described in Eq. (30) to determine the flow temperature and velocity.

VI. Results of Analysis Algorithm

To evaluate the precision of the interferogram processing routine, synthetic interferograms (see Sec. IV) of known characteristics will be used. These interferograms have been generated such that they have the same order of magnitude in annulus width, annulus radii, and SNR as the experimental ones obtained with the setup being currently used in the Laboratory [29–31]. For the interferogram generation, given values for N_E and φ_0 and for f_f are prescribed; the robustness of the algorithm is thus estimated by the relative errors between the values derived from interferogram analysis and these reference values.

A. Simulation Parameters

1. Setup

The camera resolution Res and the optical f_f and interferometer (N_E, d, λ_0, μ) parameters are chosen to simulate a previous experiment [29]. The focal length $f_f = 300$ mm and the interferometer parameters are used to define the instrument function I_{FP}, from Eqs. (12) and (15). The mirrors of the interferometer considered here have a reflectivity of $89 \pm 1\%$ at the laser wavelength $\lambda_0 = 532$ nm. This corresponds to a finesse $N_E = 26^{+3,8}_{-1,5}$ [25]. The value of N_E chosen for the simulated interferograms is thus 26. The separation between the mirrors is $d = 20$ mm.

2. Reference Interferogram Generation

To generate the reference interferogram on a mesh corresponding to the camera resolution, one needs to mimic the integration effect on the camera pixels, due to the finer scales of the interferogram features, compared to the pixel size. It is revealed by an apparent decrease of the maximum intensity as one goes from one fringe to another one of larger diameter. At first, the interferogram is built on a finer mesh, introducing a submesh of 40×40 subpixels for each camera pixel, so that the gradient of intensity is small in each subpixel. Equation (16) is evaluated at the corresponding radius of each point of this grid. For each camera pixel (X, Y), the intensity $I^{2D}_{\text{FP}}(X, Y)$ is then obtained by averaging the values over the submesh.

3. Rayleigh Interferograms Generation

Three sets of synthetic Rayleigh scattering spectra S_R are generated, by considering that the diffusing molecules are those of an isothermal medium at atmospheric pressure and at a fixed temperature $T_0 = 293$ K. The medium is considered either at rest ($u_1 = 0$ m/s) or at high subsonic speed ($u_2 = 260$ m/s and $u_3 = u_2 + 1$ m/s). The objective behind the use of these two values with a relative change below 0.4% is to assess the precision of the algorithm in the determination of the velocity. For each spectrum (or, equivalently, for each flow condition), the intensity function as modeled in Eq. (11) is evaluated. On this basis, for each flow condition, an interferogram is generated by discretizing the intensity function over the grid corresponding to the camera sensor, and weighted with W, as defined in Eq. (19) and represented in Fig. 11 to generate Rayleigh interferograms [Eq. (20)].

B. Reference Interferogram Analysis

The parameter of the annular summing procedure used to obtain the one-dimensional data set $\tilde{I}_{\text{FP}}$ from the reference interferogram is R_1, the radius of the first annular region used in the annular summing, as defined in Eq. (21). For a given interferogram, the procedure to identify the instrument function described in Sec. V.B is applied here for values of R_1 in the range $[2p; 25p]$, p being the pixel length. The values for the finesse and the phase that are determined as the result of this procedure, noted N_E^{id} and phase φ_0^{id}, are compared to the

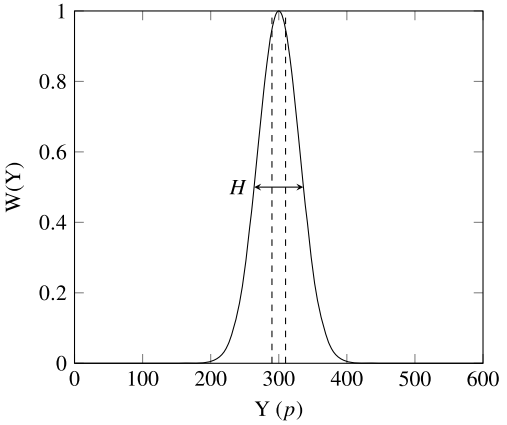

Fig. 11 Cross-section of the laser beam intensity distribution with $\sigma \simeq 0.2 \times 10^{-3}$ m. The dashed lines correspond to a truncation window of 20 p height.

prescribed (known) values N_E and φ_0. As the phase is defined modulo 2π, the relative error on the phase is calculated using to the rest modulo 2π of the prescribed value, noted $\varphi_0^{(\mathrm{mod}\,2\pi)}$. The synthetic interferograms are generated without added noise, because the SNR is expected to be really high (SNR≈1500) in experiments devoted to the instrument characterization, before flow measurements. Figure 12 shows the evolution of N_E^{id} and φ_0^{id}, provided by Eq. (29) with R_1/p. The relative error on N_E^{id} monotonically decreases as R_1/p decreases, this trend being modulated by estimation noise. The relative error asymptotically reaches 0.08%, which is only one order of magnitude smaller than that obtained typically for $R_1/p \simeq 25$. The main identified cause for this bias is the integration effect on the pixel, as discussed in Sec. VI.A; similar behavior is observed for φ_0^{id} estimation, as plotted in Fig. 12b. However, the error committed on the estimate of φ_0 is contained within a small interval below 0.2%. From these results, we conclude that any value of $R_1/p \leq 10$ is suitable for this reference interferogram analysis. Note that the annular summing procedure chosen here would be equivalent to a pixel-by-pixel approach if R_1/p is sufficiently small.

C. Rayleigh Interferogram Analysis

According to the optical setup considered in Fig. 4, the object and image planes are conjugated. The velocity and temperature estimate derived from the analysis of one part of the truncated interferogram would thus correspond to the local values of these parameters in the conjugated area of the object plane. The smaller the area analyzed in the interferogram, the higher the spatial resolution. In what follows, the first peak of the truncated interferogram is analyzed to ensure a small probed volume. There are two main causes of error in this analysis. The first one would be an error in the determination of the interferometer instrument function. At first order, a bias in the determination of the finesse would lead to an error in the temperature estimation, and an error in the determination of φ_0^{id} would lead to an error in the velocity estimation. A second cause of error would be the analysis of the Rayleigh interferogram itself, which presents two major differences compared with the reference interferogram: first, the data are confined to a restricted area of the interferogram (see Fig. 5c), which means that the averaging process of the data will rely on fewer samples over the image plane than the reference interferogram, as described in Sec. V, and second, the SNR is much lower. These two differences are discussed in what follows. The prescribed instrument function is used so that there is no cause of error other than image processing and SNR.

1. *Truncation Effect*

As the light source intensity is not uniform over the truncated interferogram, we investigate the possible bias induced on the analysis outcome. A comparative study was performed with a 20 p height truncation window, on interferograms from the spatially uniform source as in Fig. 5b and the laser-shaped source as in Fig. 5c. The maximum difference in the relative error on the temperature between the two interferograms is 0.44%. Consequently, for the ease of the forthcoming discussion, the analysis will focus on interferograms obtained from a spatially uniform broadband source, as shown in Fig. 5b. Three different truncations of this interferogram are performed, with heights $h_1 = 600p$ (no truncation), $h_2 = 40p$, and $h_3 = 20p$, the latter corresponding to approximately $H/3$. The sensitivity analysis of the procedure to R_1/p is performed on truncated interferograms using the prescribed instrument function. The results are showed in Fig. 13 Considering first the results obtained with h_1, we observe that the relative error on the temperature follows a similar evolution than for N_E^{id}, which corresponds to a bias due to the spatial averaging. The error for small values of R_1/p is two orders of magnitude lower than that obtained for $R_1/p \simeq 60$.

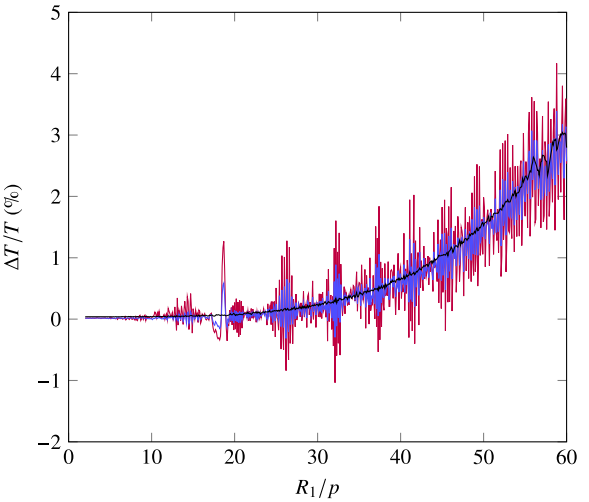

Fig. 13 Relative error on the temperature estimation for varying bin size. Truncation window height: – h_3, – h_2, – h_1.

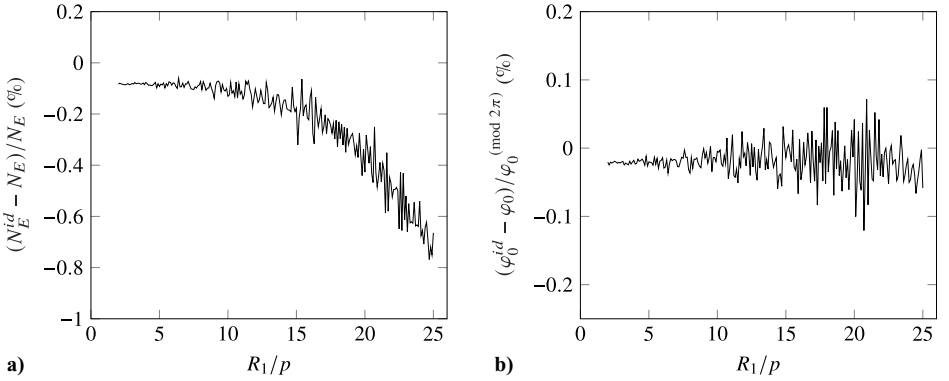

Fig. 12 Relative error of the instrument function parameters for varying R_1 a) N_E^{id}, b) φ_0^{id}.

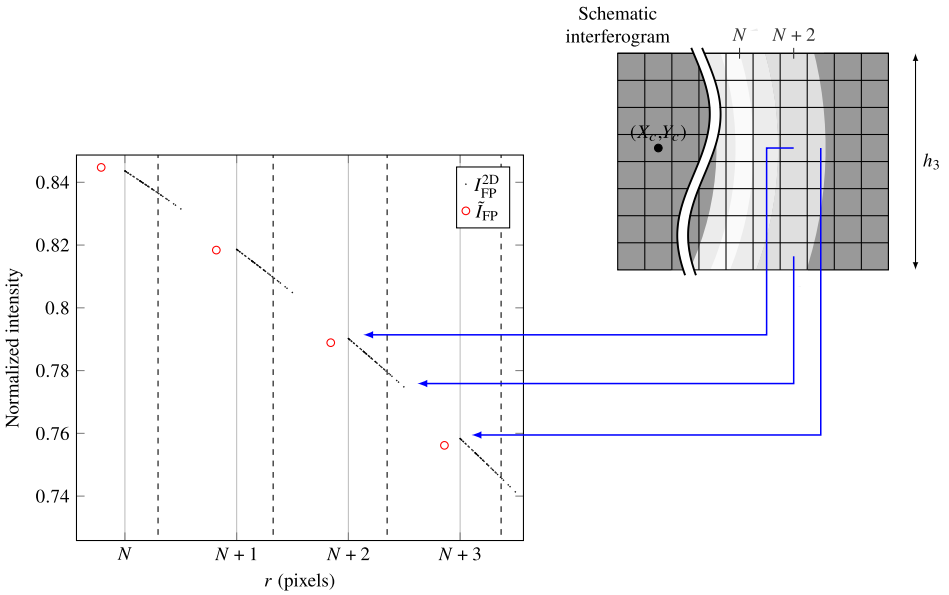

Fig. 14 Instrument function I_{FP}^{2D} for every pixel on the interferogram and $\tilde{I}_{FP}$ from the annular summing procedure, on the right side of the first peak. The dashed lines denote the values of R_i [Eq. (21), with $R_1/p = 18.2$].

The results obtained for truncation windows height h_2 and h_3 follows the trend of the full interferogram, but with increased sensitivity to small variations of R_1/p. In addition, the uncertainty of the results is increased around several values of R_1/p, the three first being $R_1/p = 18.2, 26.2, 31.5$. The ratio of the successive values to the first one increases as $\sqrt{q}$, $q \in \mathbb{N}^*$. Indeed, the annular regions obtained with these values of R_1/p encompass one another. For instance, the first annular region obtained with $R_1/p = 26.2$ exactly covers the two first obtained with $R_1/p = 18.2$, the second one covers the third and the fourth, and so on. Therefore, any bias in the analysis due to the annular summing is repeated for these particular values of R_1/p. To explain this behavior, one investigates the case $R_1/p = 18.2$, by comparing in Fig. 14 the approximate intensity function obtained with annular summing, and the data set corresponding to the intensity of each pixels over the truncated interferogram. The portion of the truncated interferogram corresponds to the outer part of the first peak. It can be seen that, because of the value oh h_3, data are scarce and there are intervals of r over which no data are available. Applying the annular summing procedure with $R_1/p = 18.2$ in this case leads to a systematic underestimation of the intensity and thus a bias in the temperature estimate.

2. *Noise Effect*

The effect of a moderate SNR on the accuracy of u and T estimates is investigated. In an experimental context with nonintensified cameras capturing Rayleigh scattered light induced by 5 W incident illumination, preliminary measurements showed that a SNR of 3 can be expected. Several interferograms with added noise are computed to establish a statistical estimation of the procedure's sensibility to the image quality. The generated noise is random with a uniform distribution, and a set of 100 interferograms is generated, over which a statistics on temperature and velocity estimates will be evaluated to determine the effects of noise, considering interferograms with SNR of 3. The noise floor level constant N_F is set here to zero.

The standard deviation of the relative error on temperature σ_T and velocity σ_u obtained from 100 interferograms is displayed in Fig. 15. Over the whole range of R_1/p, the trends are similar for σ_T and σ_u; unexpectedly, σ_T is approximately two times higher than σ_u. The standard deviation for both quantity peaks for small values of R_1/p and slightly increases with this parameter above $R_1/p \approx 17$, within the range tested here. One might expect the standard deviation to keep increasing as R_1/p increases further. For low values of R_1/p, annular averages are calculated on a small number of samples, similar to what was detailed in Sec. VI.C.1. On one hand, for a given annular region, averages are therefore subject to strong variations from one image to another, with noise contributing differently to the average value in this region. On the other hand, for a given image, the averages over successive annular regions can be very different due to the various contributions of noise. As a result, in the case of interferograms with moderate SNR, a sufficient number of points need to be averaged in each annular region describing the zone under analysis (in this case, the first peak). For the interferograms analyzed here, this condition is met for a R_1/p value of at least 17. Reducing the sensitivity of Rayleigh scattering measurement results is therefore one of the benefits of the annular summing approach; the analysis carried out here identifies that, for a Rayleigh interferogram, there is a range of values for R_1/p that enables the dispersion of results to be minimized.

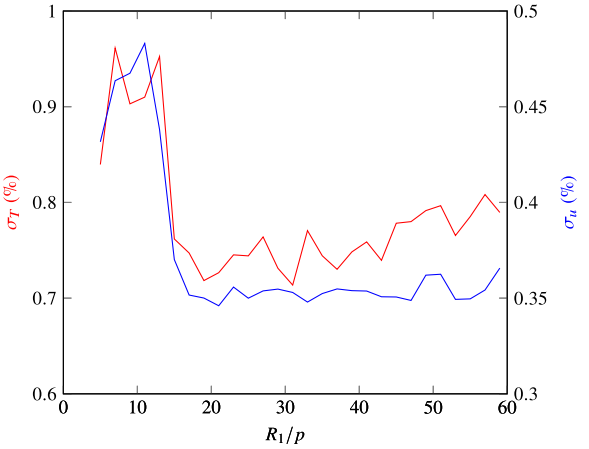

Fig. 15 Standard deviation of the relative error on temperature σ_T and velocity σ_u obtained from 100 interferograms, for varying bin size.

Looking at the results of Figs. 13 and 15, the value of R_1/p is a result of a compromise. It must be chosen small enough to avoid overestimation of T and high enough so that σ is minimized for noisy interferograms.

3. *Estimations of Temperature and Velocity for Different Test Cases*

Table 1 shows the results of the procedure applied to three simulated flow conditions. The procedure is first carried out using the analytical curve from Eq. (11), but also independently from the interferogram, with $R_1/p = 30$. Each input (curve or interferogram) is then analyzed with the prescribed instrument function, directly derived from the analytical model with the true values of the parameters

Table 1 Results of the fitting procedure from analytical curve and image processing for three flow conditions

Instrument function	u_1, m/s	T_0, K	u_2, m/s	T_0, K	u_3, m/s	T_0, K
Analytical curve						
Prescribed	0.00	293.00	260.00	293.00	261.00	293.00
Identified	0.00	292.92	260.00	292.92	261.00	292.92
Interferogram						
Prescribed	−1.32	290.01	260.37	293.96	262.13	292.20
Identified	−1.25	290.24	260.39	293.56	262.12	291.30

used to generate the interferograms (path 2 in Fig. 10), and the identified instrument function, corresponding to the instrument function whose parameters are derived from the minimization procedure (29) (path 1 in Fig. 10). As can be expected, the error is lower when analyzing the analytical curve. With the prescribed instrument function, the flow characteristics are found with negligible error. Using the identified instrument function, the error on velocity is less than $0.1\ \mathrm{m}\cdot\mathrm{s}^{-1}$, and the error on temperature is around 0.08 K, whatever the velocity considered. Image processing induces a slight bias in the estimation of flow parameters. With the prescribed instrument function, the error on velocity is around 1 m/s and at most 3 K for temperature. The temperature and velocity error are of the same order with the identified instrument function. Note that the values displayed in the last two rows of Table 1 are not to be taken as absolute. These are mere typical values, obtained from interferograms with a single value of φ_0 and a given noise distribution; these values can vary according to the noise distribution and interferogram characteristics. Nevertheless, these results indicate that the image processing, that is, annular summing and truncation of the interferogram, or image quality, SNR, and pixel integration effects, are the main causes of error in the estimation of the temperature and velocity. The error committed by using the identified instrument function to analyze the interferograms rather than the prescribed instrument function is of second order.

VII. Conclusions

A new analysis of Fabry–Pérot interferograms from Rayleigh scattered light is presented to determine the velocity u and the temperature T, at a point probe in a flow. The interferograms are here converted into intensity functions using annular summing, to overcome inherent issues of pixel by pixel scrutiny. First, for a monochromatic source, these functions are examined using an original analytical formulation, completed by an optimization procedure. Second, the Rayleigh interferograms are truncated to take the laser beam shape into account. The resulting intensity functions have been processed using an iterative procedure, relying on the Tenti S6 scattering model. The lack of literature regarding errors in interferogram analysis and the need to understand their source is of primary interest to get reliable measurements. To address this, a methodology is thus developed using synthetic interferograms that simulate realistic experimental conditions. The investigation of these synthetic interferograms allows for the understanding of the intrinsic biases of the processing and the estimation of the maximum achievable precision of this method without experimental errors. The two instrument function parameters were found with less than 0.1% relative error for both the finesse N_E and the phase φ_0. Noise has been added in the interferograms to assess the robustness of the processing with added noise. The standard deviation of the relative error on T and u are found to be as low as 0.75 and 0.35%, respectively, for $R_1/p = 30$. The annular summing procedure is shown to be equivalent to pixel-by-pixel analysis for the reference interferogram. However, the standard deviation of the relative error on noisy Rayleigh interferograms is reduced with the present method. Experimental results obtained with the optical described in this study have been processed with success.

Appendix: Analytical Development on the Finesse

Equation (28) providing expression of finesse N_E is established here. At half intensity when $I_{FP} = I_0/2$, the term $(2N_E/\pi)^2 \sin^2(\varphi/2)$ in Eq. (14) takes the value 1. Hence,

$$\sin(\varphi/2) = \pi/(2N_E) \tag{A1}$$

Considering only the first intensity peak, two solutions denoted φ_{1^-} and φ_{1^+} are found on each side of this peak,

$$\begin{cases} \varphi_{1^-} = -2\arcsin[\pi/(2N_E)] \\ \varphi_{1^+} = 2\arcsin[\pi/(2N_E)] \end{cases} \tag{A2}$$

Expressing the phase from the radius on the intensity function, one obtains

$$\begin{cases} \varphi_{1^-} = \varphi_0\left(1 - \dfrac{1}{2}\dfrac{r_{1^-}^2}{f_f^2}\right) = -2\arcsin[\pi/(2N_E)] \\ \varphi_{1^+} = \varphi_0\left(1 - \dfrac{1}{2}\dfrac{r_{1^+}^2}{f_f^2}\right) = 2\arcsin[\pi/(2N_E)] \end{cases} \tag{A3}$$

Then, isolating the radius in both expressions provides

$$\begin{cases} r_{1^-}^2 = \left(1 + \dfrac{8}{\varphi_0}\arcsin\left(\dfrac{\pi}{2N_E}\right)\right) f_f^2 \\ r_{1^+}^2 = \left(1 - \dfrac{8}{\varphi_0}\arcsin\left(\dfrac{\pi}{2N_E}\right)\right) f_f^2 \end{cases} \tag{A4}$$

and by subtracting these two equations, one gets

$$\frac{r_{1^+}^2 - r_{1^-}^2}{f_f^2} = \frac{8}{\varphi_0}\arcsin\left(\frac{\pi}{2N_E}\right)\frac{\pi}{2N_E} \tag{A5}$$

This expression can be recast to extract N_E,

$$\sin\left(\frac{r_{1^+}^2 - r_{1^-}^2}{f_f^2}\frac{\varphi_0}{8}\right) = \frac{\pi}{2N_E} \tag{A6}$$

and the finesse reads as

$$N_E = \frac{\pi}{2\sin[(\varphi_0/8)(r_{1^+}^2 - r_{1^-}^2/f_f^2)]} \tag{A7}$$

By definition, the term $r_{1^+}^2 - r_{1^-}^2$ takes the form

$$\begin{aligned} r_{1^+}^2 - r_{1^-}^2 &= (r_1 + \mathrm{FWHM}_1/2)^2 - (r_1 - \mathrm{FWHM}_1/2)^2 \\ &= 2r_1\mathrm{FWHM}_1 \end{aligned} \tag{A8}$$

and by substituting this expression into Eq. (A7), Eq. (28) of the main text is obtained, namely,

$$N_E = \frac{\pi}{2\sin[(\varphi_0/4)(r_1^\star \mathrm{FWHM}_1/f_f^2)]}$$

Acknowledgments

This work was performed within the framework of the industrial chair ARENA (grant number ANR-18-CHIN-0004-01) cofinanced by Safran Aircraft Engines and the French National Research Agency and in the framework of the Labex CeLyA (grant number ANR-10-LABX-0060) of the University of Lyon, within the program "Investissements d'Avenir" (grant number ANR-16-IDEX-0005) operated by the French National Research Agency.

References

[1] Mercier, B., Jondeau, E., Castelain, T., Ozawa, Y., Bailly, C., and Comte-Bellot, G., "High Frequency Temperature Fluctuation Measurements by Rayleigh Scattering and Constant-Voltage Cold-Wire Techniques," *Experiments in Fluids*, Vol. 60, No. 7, 2019, p. 110. https://doi.org/10.1007/s00348-019-2753-y

[2] Mielke, A. F., "Development of a Molecular Rayleigh Scattering Diagnostic for Simultaneous Time-Resolved Measurement of Temperature, Velocity, and Density," Ph.D. Dissertation, Case Western Reserve Univ., Cleveland, OH, 2008.

[3] Seasholtz, R. G., Buggele, A. E., and Reeder, M. F., "Flow Measurements Based on Rayleigh Scattering and Fabry-Perot Interferometer," *Optics and Lasers in Engineering*, Vol. 27, No. 6, 1997, pp. 543–570. https://doi.org/10.1016/S0143-8166(96)00063-2

[4] Panda, J., "Spectrally-Resolved Rayleigh Scattering to Measure Velocity, Temperature, Density, and Density Fluctuations in High-Speed Flows," *Experiments in Fluids*, Vol. 61, No. 3, 2020, pp. 1–16. https://doi.org/10.1007/s00348-020-2903-2

[5] Mielke, A. F., Seasholtz, R. G., Elam, K. A., and Panda, J., "Time-Average Measurement of Velocity, Density, Temperature, and Turbulence Velocity Fluctuations Using Rayleigh and Mie Scattering," *Experiments in Fluids*, Vol. 39, No. 2, 2005, pp. 441–454. https://doi.org/10.1007/s00348-005-0990-8

[6] Panda, J., and Seasholtz, R., "Velocity and Temperature Measurement in Supersonic Free Jets Using Spectrally Resolved Rayleigh Scattering," *37th Aerospace Sciences Meeting and Exhibit*, AIAA Paper 1999-0296, 1999. https://doi.org/10.2514/6.1999-296

[7] Mercier, B., Castelain, T., Jondeau, E., and Bailly, C., "Density Fluctuations Measurement by Rayleigh Scattering Using a Single Photomultiplier," *AIAA Journal*, Vol. 56, No. 4, 2018, pp. 1310–1316. https://doi.org/10.2514/1.J056507

[8] Fagan, A. F., Clem, M. M., and Elam, K. A., "Improvement in Rayleigh Scattering Measurement Accuracy," *50th AIAA Aerospace Sciences Meeting Including the New Horizons Forum and Aerospace Exposition*, AIAA Paper 2012-1060, 2012. https://doi.org/10.2514/6.2012-1060

[9] Chen, L., Yang, F. R., Su, T., Bao, W. Y., Yan, B., Chen, S., and Li, R. B., "High Sampling-Rate Measurement of Turbulence Velocity Fluctuations in Mach 1.8 Laval Jet Using Interferometric Rayleigh Scattering," *Chinese Physics B*, Vol. 26, No. 2, 2017, Paper 025205. https://doi.org/10.1088/1674-1056/26/2/025205

[10] Cutler, A. D., Rein, K., Roy, S., Danehy, P. M., and Jiang, N., "100-kHz Interferometric Rayleigh Scattering for Multi-Parameter Flow Measurements," *Optics Express*, Vol. 28, No. 3, 2020, pp. 3025–3040. https://doi.org/10.1364/OE.380934

[11] Estevadeordal, J., Jiang, N., Cutler, A. D., Felver, J. J., Slipchenko, M. N., Danehy, P. M., Gord, J. R., and Roy, S., "High-Repetition-Rate Interferometric Rayleigh Scattering for Flow-Velocity Measurements," *Applied Physics B: Lasers and Optics*, Vol. 124, No. 3, 2018, pp. 1–6. https://doi.org/10.1007/s00340-018-6908-y

[12] Bivolaru, D., Cutler, A., and Danehy, P., "Spatially- and Temporally-Resolved Multi-Parameter Interferometric Rayleigh Scattering," *49th AIAA Aerospace Sciences Meeting Including the New Horizons Forum and Aerospace Exposition*, AIAA Paper 2011-1293, 2011. https://doi.org/10.2514/6.2011-1293

[13] Sheng, W., Jin-Hai, S., Jun, S., Zhi-yun, H., Jing-feng, Y., and Jing-Ru, L., "Two-Dimensional Interferometric Rayleigh Scattering Velocimetry Using Multibeam Probe Laser," *Optical Engineering*, Vol. 56, No. 11, 2017, pp. 11,1705–11,1705. https://doi.org/10.1117/1.oe.56.11.111705

[14] Panda, J., and Seasholtz, R. G., "Experimental Investigation of Density Fluctuations in High-Speed Jets and Correlation with Generated Noise," *Journal of Fluid Mechanics*, Vol. 450, Jan. 2002, pp. 97–130. https://doi.org/10.1017/S002211200100622X

[15] Mercier, B., Castelain, T., and Bailly, C., "Experimental Investigation of the Turbulent Density–Far-Field Sound Correlations in Compressible Jets," *International Journal of Aeroacoustics*, Vol. 17, Nos. 4–5, 2018, pp. 521–540. https://doi.org/10.1177/1475472X18778274

[16] Mielke, A. F., and Elam, K. A., "Dynamic Measurement of Temperature, Velocity, and Density in Hot Jets Using Rayleigh Scattering," *Experiments in Fluids*, Vol. 47, Nos. 4–5, 2009, pp. 673–688. https://doi.org/10.1007/s00348-009-0708-4

[17] Mielke-Fagan, A. F., Clem, M. M., and Elam, K. A., "Rayleigh Scattering Measurements Using a Tunable Liquid Crystal Fabry-Perot Interferometer," *27th AIAA Aerodynamic Measurement Technology and Ground Testing Conference 2010*, AIAA Paper 2010-4350, 2010. https://doi.org/10.2514/6.2010-4350

[18] Coakley, M. M., Roesler, F. L., Reynolds, R. J., and Nossal, S., "Fabry–Perot CCD Annular-Summing Spectroscopy: Study and Implementation for Aeronomy Applications," *Applied Optics*, Vol. 35, No. 33, 1996, pp. 6479–6493. https://doi.org/10.1364/ao.35.006479

[19] Miles, R. B., Lempert, W. R., and Forkey, J. N., "Laser Rayleigh Scattering," *Measurement Science and Technology*, Vol. 12, No. 5, 2001, Paper R33. https://doi.org/10.1088/0957-0233/12/5/201

[20] Tenti, G., Boley, C. D., and Desai, R. C., "On the Kinetic Model Description of Rayleigh–Brillouin Scattering from Molecular Gases," *Canadian Journal of Physics*, Vol. 52, No. 4, 1974, pp. 285–290. https://doi.org/10.1139/p74-041

[21] Sutherland, W., "LII. The Viscosity of Gases and Molecular Force," *London, Edinburgh, and Dublin Philosophical Magazine and Journal of Science*, Vol. 36, No. 223, 1893, pp. 507–531. https://doi.org/10.1080/14786449308620508

[22] Mielke, A. F., Elam, K. A., and Sung, C.-J., "Rayleigh Scattering Diagnostic for Measurement of Velocity and Density Fluctuation Spectra," *40th AIAA Aerospace Sciences Meeting and Exhibit*, AIAA Paper 2006-0827, 2006. https://doi.org/10.2514/6.2002-827

[23] Gu, Z., Witschas, B., van de Water, W., and Ubachs, W., "Rayleigh–Brillouin Scattering Profiles of Air at Different Temperatures and Pressures," *Applied Optics*, Vol. 52, No. 19, 2013, pp. 4640–4651. https://doi.org/10.1364/AO.52.004640

[24] Mielke, A. F., Elam, K. A., and Clem, M. M., "Multiple-Point Mass Flux Measurement System Using Rayleigh Scattering," *47th AIAA Aerospace Sciences Meeting Including the New Horizons Forum and Aerospace Exposition*, AIAA Paper 2009-0528, 2009. https://doi.org/10.2514/6.2009-528

[25] Vaughan, J. M., *The Fabry–Perot Interferometer*, Routledge, New York, 2017. https://doi.org/10.1201/9780203736715

[26] Makela, J. J., Meriwether, J. W., Huang, Y., and Sherwood, P. J., "Simulation and Analysis of a Multi-Order Imaging Fabry-Perot Interferometer for the Study of Thermospheric Winds and Temperatures," *Applied Optics*, Vol. 50, No. 22, 2011, pp. 4403–4416. https://doi.org/10.1364/AO.50.004403

[27] Atherton, T. J., and Kerbyson, D. J., "Size Invariant Circle Detection," *Image and Vision Computing*, Vol. 17, No. 11, 1999, pp. 795–803. https://doi.org/10.1016/S0262-8856(98)00160-7

[28] Pan, X., Shneider, M. N., and Miles, R. B., "Coherent Rayleigh-Brillouin Scattering," *Physical Review Letters*, Vol. 89, No. 18, 2002, pp. 1–4. https://doi.org/10.1103/PhysRevLett.89.183001

[29] Kurek, I., "Mesures de Vitesse, Température et Masse Volumique Par Diffusion Rayleigh et Étude de l'effet de Vol Sur Les Ondes Guidées Dans Des Jets Subsoniques," Ph.D. Dissertation, Central School of Lyon, Écully, France, Jan. 2024.

[30] Kurek, I., Castelain, T., Lecomte, P., Jondeau, E., and Bailly, C., "Mesures de Vitesse et de Température par Diffusion Rayleigh, Acquisition Simultanée de la Fonction D'instrument et de la Lumiére Diffusée," *18ème Congrès Françophone de Techniques Laser*, 2024.

[31] Castelain, T., Kurek, I., Lecomte, P., and Bailly, C., "Turbulence Analysis from Long-Exposure-Time Acquisitions with Interferometric Rayleigh Scattering," *21st International Symposium on Application of Laser and Imaging Techniques to Fluid Mechanics*, 2024.

L. Ukeiley
Associate Editor